

THERMAL MANAGEMENT OF INTEGRATED PUMP MOTORS: DESIGN AND VALIDATION

Su, X. Z.^{*,**}; Zhou, L.^{*#}; Yan, H.^{***} & Zhang, H.^{***}

^{*} Jiangsu University, Zhenjiang 212013, China

^{**} City University of Hefei, Hefei 230009, China

^{***} Hefei University of Technology, Hefei 230009, China

E-Mail: 2112511130@stmail.ujs.edu.cn ([#] Corresponding author)

Abstract

This study investigates the temperature rise characteristics of permanent magnet synchronous motors (PMSMs) for integrated pumps under high-power-density operation. Losses were calculated using Joule's law and the Bertotti iron loss separation model. Computational fluid dynamics (CFD) simulations of multiple primary-secondary channel configurations were conducted to analyse flow velocity, pressure, and temperature field distributions. An experimental test bench was built for validation. Simulation and experimental results show that the full-spiral primary channel combined with a radial Z-shaped secondary channel (right inlet/left outlet) yields optimal cooling. Additionally, under typical engineering parameters, the maximum winding temperature was reduced to 49.6 °C. Notably, under rated conditions, the simulated winding temperature deviates by only 0.8 % from measurements, with all key parameter errors below 8 %, and the cooling structure ensures stable motor operation under overload. This study provides a theoretical and experimental basis for designing efficient cooling systems for compact, high-power-density PMSMs in integrated pumps.

(Received in December 2025, accepted in April 2026. This paper was with the authors 2 months for 2 revisions.)

Key Words: Integrated Pump, Fluid–Structure Interaction (FSI), Experimental Validation

1. INTRODUCTION

Integrated pumps, integrating the pump and motor into a single compact unit, offer high power density and superior system efficiency, facilitating their widespread adoption in new energy vehicles and aerospace [1, 2]. A key challenge lies in the thermal management of their interior permanent magnet synchronous motors (PMSMs). The confined internal space, concentrated heat sources, and limited heat dissipation pathways create a critical thermal bottleneck: during sustained high-power operation, ineffective dissipation of copper and iron losses leads to excessive temperature rise, degrading permanent magnet properties, accelerating insulation aging, and compromising the reliability, efficiency, and service life of the entire system [3, 4]. Thus, excessive temperature rise in PMSMs critically constrains further improvements in power density and compactness for integrated pump technology.

Liquid cooling, characterized by its compact form factor and excellent heat transfer capability, is widely adopted for high-power-density motors [5]. Cooling channel design – specifically its geometry and flow path – is paramount, as it directly governs coolant distribution and heat exchange efficiency, which ultimately dictates the system's cooling performance and pumping power. However, existing studies predominantly focus on single-channel spiral or zigzag configurations, which are effective only in specific layouts. In complex multichannel networks, inadequate coordination between coolant distribution and pressure balance stagnates flow in secondary channels, impairing local heat transfer. Moreover, most simulations rely on steady-state assumptions, failing to accurately capture transient flow-thermal dynamics. Experimental validation is often limited to rated operating conditions, leaving a gap in defining safe thermal boundaries under extreme peak-power scenarios – a shortfall that poses unforeseen overheating risks in practical applications.

2. STATE OF THE ART

Advancements in integrated pump technology demand stringent thermal management of PMSMs, prompting extensive research on motor cooling, especially liquid cooling system optimization. These efforts have yielded significant progress yet uncovered critical challenges warranting further investigation.

Motor loss modelling and calculation underpin thermal dissipation design, yet existing frameworks lack adaptability to PMSMs for integrated pumps. Some researchers have enhanced loss calculation methods and thermal prediction accuracy [5, 6], while others explored practical applications and theoretical foundations of loss modelling [7-9]. Yu et al. [7], for instance, clarified how loss distribution affects motor thermal performance, offering a reference for subsequent studies. However, these investigations primarily target conventional PMSMs under normal operating conditions, rendering them ill-suited to the inherent characteristics of integrated pump PMSMs – namely high-speed, high-load operation and concentrated heat sources. Time-varying and nonlinear loss modelling remains incomplete, with no coupled analysis incorporating cooling channels. Consequently, these studies fail to provide a reliable thermal foundation for heat dissipation design in integrated pump PMSMs.

Optimization of cooling channel configurations is key to enhancing thermal dissipation efficiency. However, existing studies focus predominantly on single-channel designs, overlooking the synergistic design of primary and secondary channels required for the confined space of integrated pumps. Previous work has optimized individual cooling circuits [10-14]: Jenkins et al. [10] introduced a novel liquid cooling configuration, while Xie et al. [11] refined oil injection tube cooling structures, advancing single-circuit design methodology. Nevertheless, these studies overlooked both the spatial constraints of integrated pumps and the need for synergistic primary–secondary channel design. Consequently, they failed to resolve issues such as uneven coolant distribution and flow dead zones, rendering them inadequate for achieving efficient and uniform thermal dissipation.

With advances in computer technology, fluid–structure interaction (FSI) simulation based on computational fluid dynamics (CFD) and the finite element method has become a core approach for cooling system design and performance prediction. Numerous CFD studies have focused on developing thermal network models [15], optimizing cooling structure simulations [16], refining simulation methodologies [17, 18], and expanding application scenarios [19, 20]. Gözüaçık and Akar [21] developed a multi-physics and electromagnetic–thermal–fluid coupled design framework to optimize high-performance PMSMs, providing a critical reference for integrated pump motor simulations. However, when applied to integrated pump PMSMs, existing simulation studies often involve excessive model simplification – neglecting secondary cooling channels, adopting equivalent winding models, or evaluating performance only at a single design point. This lack of systematic comparison among various primary–secondary channel configurations across the full operating range renders such studies insufficient for guiding the optimal engineering design of integrated pump PMSMs.

Experimental testing constitutes the ultimate step for validating theoretical and simulation results. Zhao and Yu [22] analysed the correlation between permanent magnet demagnetization and motor temperature rise, providing critical supporting evidence for parameter determination and result interpretation in PMSMs thermal testing. Han et al. [23] conducted thermal tests on high-speed motors for magnetically suspended control moment gyroscopes and established a high-precision methodology for loss measurement and temperature rise characterization. However, existing experiments predominantly focus on steady-state tests under rated operating conditions. Consequently, sufficient experimental data and quantitative evaluation remain lacking regarding the transient thermal response, ultimate heat dissipation capacity of cooling systems, and long-term thermal cycling reliability of integrated pump

PMSMs under demanding operational conditions – such as peak torque, peak speed, and variable duty cycles – encountered in practical applications. This shortfall results in some cooling designs meeting standard testing requirements yet facing overheating risks under actual complex operating conditions.

Therefore, this study establishes an accurate multiphysics loss model for the motor. Employing CFD-based FSI simulation, it investigates the flow characteristics, pressure distribution, and temperature field under various primary-secondary channel configurations, thereby revealing the synergistic mechanism by which primary and secondary channels influence heat dissipation performance. Subsequently, through prototype fabrication and a comprehensive experimental platform, complete performance and temperature rise tests are conducted under multiple operating conditions ranging from rated to peak torque and peak speed. This forms a closed-loop design methodology encompassing mechanism analysis, simulation optimization, and experimental validation, aimed at overcoming existing heat dissipation bottlenecks and enhancing the power density and operational reliability of integrated pump systems.

3. METHODOLOGY

3.1 Motor loss modelling and computation

To simulate motor temperature rise, it is essential to quantify internal heat sources and clarify heat transfer paths. In this study, calculation models are established for loss components of PMSMs in integrated pumps. The formulations for each loss are presented as follows:

Winding copper loss (Joule's Law):

$$P_{Cu} = \sum_{i=1}^m I_{ph}^2 R_{ph} \quad (1)$$

where m is the number of phases, I_{ph} is the phase current, R_{ph} is the phase resistance.

Core loss (Bertotti's separation model):

$$P_{Fe} = P_h + P_e + P_a = K_h f B_m^\alpha + K_e f^2 B_m^2 + K_a f^{1.5} B_m^{1.5} \quad (2)$$

where P_h represents the hysteresis loss per unit volume, P_e represents the eddy current loss per unit volume, P_a represents the excess loss per unit volume, K_h represents the hysteresis loss coefficient, f represents the frequency of the alternating current in the PMSMs, B_m represents the amplitude of the sinusoidal magnetic flux density, K_e represents the excess loss coefficient, and K_c represents the eddy current loss coefficient.

Permanent magnet eddy current loss:

$$P_{em} = \int \frac{J_n^2}{\sigma} dV \quad (3)$$

where J_n is the eddy current density and σ is the electrical conductivity of the permanent magnet.

Mechanical loss (empirical formula):

$$P_f = aL\omega_r D_s^2 \quad (4)$$

where a is an empirical coefficient, L is the effective motor length, ω_r is the angular velocity, and D_s is the outer diameter of the stator core.

Based on the aforementioned models, the losses of each component and volumetric heat generation rates of the PMSMs for integrated pumps under rated operating conditions were calculated, as presented in Table I. These losses were adopted as heat sources for subsequent CFD simulations.

Table I: Losses, volumes, and heat generation rates of motor components.

Motor component	Loss (W)	Volume (mm ³)	Heat generation rate (W/m ³)
Winding copper loss	48.5	14376.27	3373615
Stator core loss	18.6	23853.68	779753
Rotor core loss	5.2	7380.02	704607
Eddy current loss	0.9	1872.00	480769

3.2 Motor cooling system modelling

Within the motor, heat transfer is dominated by thermal conduction across the contact interfaces of interference-fitted components (e.g., between the shaft, stator, or rotor cores). The primary mode of external heat dissipation is thermal convection, which involves heat exchange between the components and the ambient air or circulating coolant. Fig. 1 illustrates the specific heat transfer pathways.

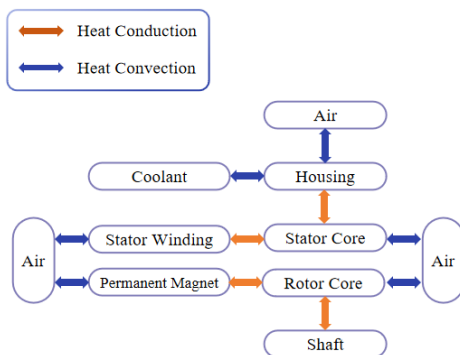


Figure 1: Schematic of heat transfer modes inside and outside the motor.

Given the motor's complex physical model, structures with negligible impact on temperature rise (e.g., fillets and ribs) are neglected, and the windings are modelled as homogeneous copper blocks. Fig. 2 shows the resulting simplified geometry.

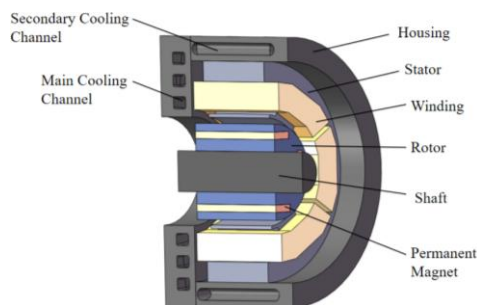


Figure 2: Layout of the cooling channels and simplified motor structure.

The cooling channel system comprises a primary cooling channel and a secondary cooling channel. Fig. 3 shows the three configurations of the primary channel: an external spiral channel, an asymmetrical spiral channel, and an internal spiral channel. Fig. 4 shows the two configurations of the secondary channel: an axial Z-shaped channel and a radial Z-shaped channel.



Figure 3: Three configurations of the primary cooling channel.



Figure 4: Two configurations of the secondary cooling channel.

3.3 Comparative analysis and simulation of cooling channel structures

Comparison of configurations with identical primary channels: In this study, an external spiral primary channel was employed in conjunction with two distinct secondary channel designs: an axial Z-shaped channel and a radial Z-shaped channel. Furthermore, three specific configurations were analysed to investigate the effects of the inlet/outlet orientation of the radial Z-shaped channel on the motor's flow velocity, pressure, and temperature distributions. Fig. 5 illustrates the configurations, and Table II details the volume of each flow channel. The total channel volumes of the three schemes are nearly identical, demonstrating a consistent basis for the subsequent temperature analysis.

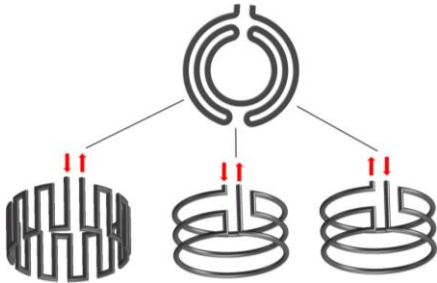


Figure 5: Schematic of the primary and secondary channel configurations.

Table II: Cooling channel structures and total channel volumes for different schemes.

Scheme	Primary and secondary channel structures	Total channel volume (mm ³)
Scheme 1	External spiral; axial Z-shaped	10113.81
Scheme 2	External spiral; radial Z-shaped (left inlet/right outlet)	8866.11
Scheme 3	External spiral; radial Z-shaped (right inlet/left outlet)	8866.11

Comparison of flow velocity distributions: A simulation analysis was performed on the three aforementioned schemes. Fig. 6 shows the velocity distribution contours for the primary and secondary cooling channels.

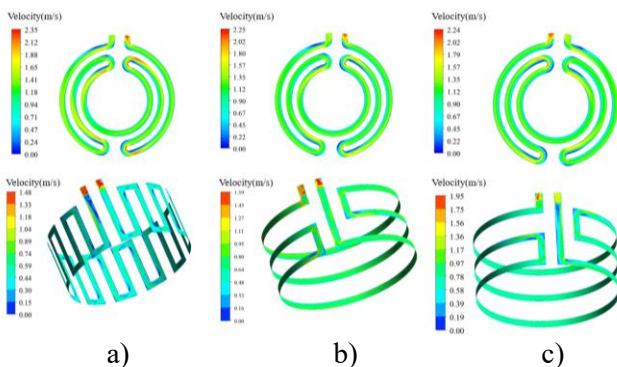


Figure 6: Velocity distribution contours for the channels of the three schemes.

The velocity distributions in the primary channels indicate that, given the identical inlet velocities and the shared external spiral structure, the flow distribution trends are similar across all three schemes. The dark blue regions represent potential flow stagnation zones

where recirculation can occur; the velocity here is extremely low, which indicates a decrease in heat transfer efficiency. As the primary channel structure is identical, these stagnation zones are located in the same positions. Furthermore, the maximum velocity in the primary channel occurs at each bend. However, the primary channel velocity in scheme 1 reached 2.35 m/s, which is higher than those in the other two types. This finding is attributed to the structure of its secondary channel, which results in increased flow resistance, consequently reducing fluid diversion from the primary channel.

The velocity distribution in the secondary channels indicates that the numerous bends in scheme 1 dissipate fluid momentum and impede flow, leading to a decrease in the maximum velocity. The average velocity was only 0.4 m/s, and the channel contained several extensive dark blue zones, which began to diminish toward the channel's centre. By contrast, the dark blue zones in the corners of scheme 2 were reduced, with the channel predominantly showing green regions, and its average velocity reached 0.85 m/s. The average velocity in the secondary cooling channel of scheme 3 was 0.78 m/s.

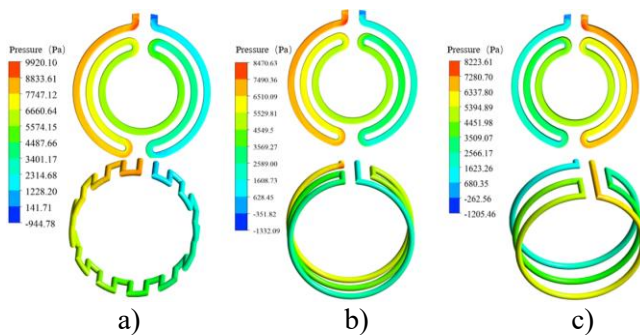


Figure 7: Pressure distribution contours for the channels of the three schemes.

Pressure distribution comparison: Fig. 7 shows that the locations of the inlet and outlet directly affect the pressure distribution within the flow channels. For all three channel schemes, the maximum and minimum pressures occurred at the bend near the inlet and outlet, respectively. The pressure was highest in the first pipe section at the inlet and decreased sequentially in the remaining sections. The pressure distributions within the primary channel were similar across all schemes because of their identical structures. In scheme 1, the numerous bends in its secondary channel increased the local flow resistance and impeded the flow, resulting in a maximum pressure of 9920.1 Pa. The maximum pressure in scheme 2 was reduced to 8470.63 Pa. Furthermore, after altering the inlet/outlet positions in scheme 3, the pressures in its primary and secondary channels decreased further, with a maximum pressure of 8223.61 Pa.

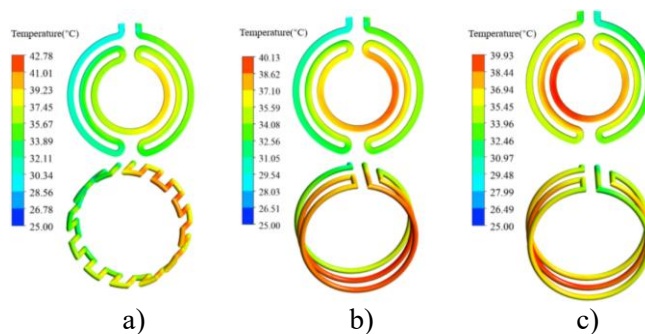


Figure 8: Temperature distribution contours for the channels of the three schemes.

Temperature distribution comparison: Fig. 8 shows similar temperature distributions within the primary channels of the three schemes, with the temperature increasing uniformly

along the flow path. For the primary and secondary channels, the majority of heat was transferred through the coolant, whereas a relatively small portion was dissipated via convection from the housing surface. The maximum temperature in scheme 1 was 42.78 °C, which was located within its secondary channel. The different inlet/outlet configurations in schemes 2 and 3 altered the locations of the high-temperature regions within the primary channel. The maximum temperature in scheme 2 was 40.13 °C and occurred in the inner section of the primary channel and the uppermost layer of the secondary channel. By contrast, scheme 3 exhibited a maximum temperature of 39.93 °C, which was primarily distributed in the inner section of the primary channel and the middle section of the secondary channel. This difference can be explained by the coolant in the secondary channel of scheme 2 flowing from bottom to top, resulting in poor cooling at the topmost section. Conversely, in scheme 3, the bottom-to-top flow in the secondary channel, positioned adjacent to the primary channel, improved heat dissipation. The lower flow velocity in the secondary channel of scheme 1 than in scheme 2 resulted in a longer fluid residence time for heat absorption, ultimately causing its maximum temperature to be 2.65 °C higher than that of scheme 2. Furthermore, changing the channel inlet/outlet positions in scheme 3 increased the flow velocity, which contributed to the reduction in the maximum and average temperatures.

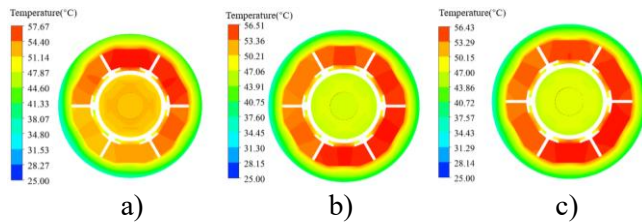


Figure 9: Temperature distribution contours of the motor for the three schemes.

The temperature distribution within the motor for each scheme was analysed to evaluate the cooling effectiveness of the three channel schemes on the motor. Fig. 9 presents distinct differences in the motor's temperature distribution for scheme 1, and the temperature distributions for schemes 2 and 3 are more uniform. Scheme 3 demonstrated superior cooling performance.

Table III: Cooling channel structures and total channel volumes for the schemes with various primary channels.

Scheme	Primary and secondary channel structures	Total channel volume (mm ³)
Scheme 1	External spiral; radial Z-shaped	8866.11
Scheme 2	Full spiral; radial Z-shaped	9005.66
Scheme 3	Internal spiral; radial Z-shaped	8849.36

Comparison of configurations with identical secondary channels but different primary channels: The radial Z-shaped secondary channel (right inlet and left outlet) was identified as the optimal cooling configuration on the basis of the previous analysis. After the secondary channel structure was fixed, the influence of different primary channel structures on the cooling performance was analysed. Altering the primary channel geometry requires the total cooling channel volumes to be approximately equal across all the designs, as significant volume differences substantially affect the motor's thermal dissipation. Table III presents the specific schemes and their corresponding channel volumes.

Velocity analysis: The average velocities for the primary and secondary channels obtained from the velocity contours were computed (Fig. 10 and Table IV). The maximum velocities in the primary cooling channels of schemes 1 and 2 were nearly identical at 2.25 m/s. The maximum velocity for scheme 3 was slightly lower at 2.12 m/s. Among the

secondary channels, scheme 2 achieved the highest maximum velocity of 2.02 m/s, whereas scheme 1 exhibited a higher secondary channel velocity than did scheme 3. Overall, the average velocities in both the primary and secondary channels of scheme 2 were greater than those of the other two schemes.

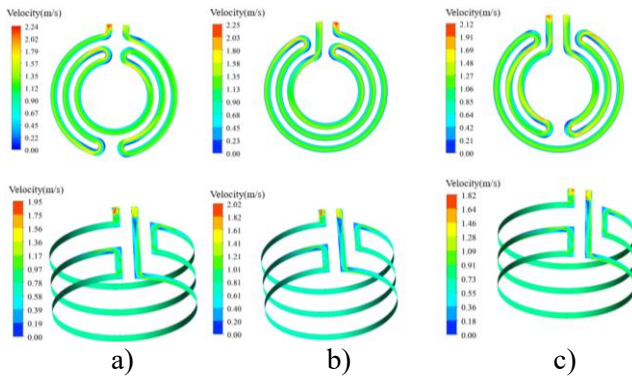


Figure 10: Velocity distribution contours for the channels of the three schemes (with various primary channels).

Table IV: Average flow velocities in the primary and secondary cooling channels for the different schemes.

Scheme	Average velocity (m/s)	
	Primary channel	Secondary channel
Scheme 1	0.83	0.69
Scheme 2	0.88	0.75
Scheme 3	0.79	0.68

Pressure analysis: The inlet pressure was higher than the outlet pressure (Fig. 11). The maximum pressure values for scheme 1, scheme 3, and scheme 2 decreased sequentially. The maximum pressure in scheme 1 was 8223.61 Pa. Scheme 2 exhibited the lowest maximum pressure of 7655.58 Pa, which can be attributed to its 6 bends, whereas the other two schemes contained 10 bends. An increase in the number of bends elevates the flow resistance, consequently increasing the pressure within the channel.

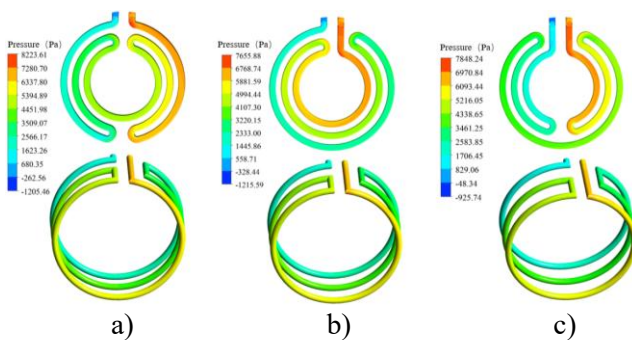


Figure 11: Pressure distribution contours for the channels of the three schemes (with various primary channels).

Temperature analysis: Scheme 2 presented the lowest temperature of 39.79 °C, indicating superior cooling performance at the channel level (Fig. 12). This trend was consistent for all the overall motor temperatures evaluated. Considering the differences in the channel pressure distribution and the resulting motor temperature field, scheme 2 achieved a maximum motor temperature of 55.18 °C, demonstrating the best cooling effectiveness, and was therefore identified as the optimal configuration.

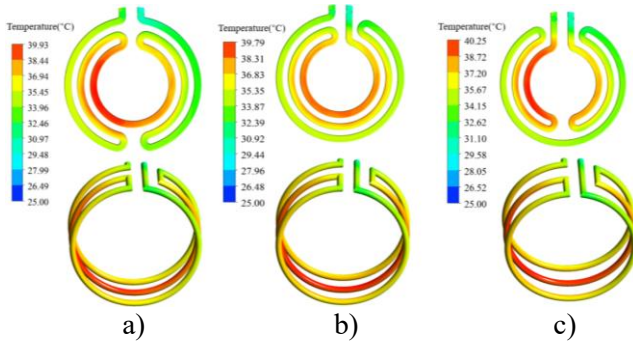


Figure 12: Temperature distribution contours for the channels of the three schemes (with various primary channels).

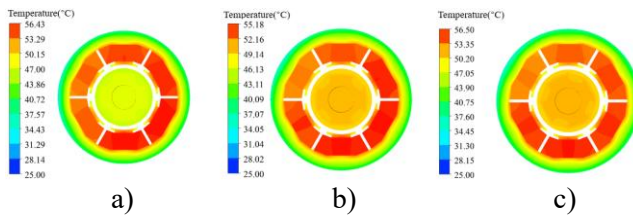


Figure 13: Temperature distribution contours of the motor for the three schemes (with various primary channels).

Comprehensive comparisons of flow velocity, pressure, and temperature distributions confirmed Configuration 2 (full-spiral primary + radial Z-shaped secondary channel, right inlet/left outlet) as the optimal cooling structure. Following typical liquid cooling design, an inlet flow rate of 2 L/min and cross-sectional dimensions $H = 4.5 \text{ mm} \times L = 3.3 \text{ mm}$ were selected. CFD simulations showed a maximum winding temperature of 49.6 °C under rated conditions, providing a theoretical basis for prototype fabrication and experimental validation.

4. EXPERIMENTAL VALIDATION

4.1 Motor parameter measurements

The key parameters of the PMSM were validated by comparing experimental measurements with finite element simulations. The back electromotive force (back-EMF) constant was measured via a no-load test method (Fig. 14). The motor under test was driven by a servomotor to a specified rotational speed, and the winding voltage was captured via an oscilloscope. The calculated back-EMF constant was 6.24 V/krpm. The phase inductance, measured via a digital LCR meter in bridge mode, was 23.55 μH . The stator phase resistance, obtained via a multimeter and a bridge method, was 0.42 Ω .

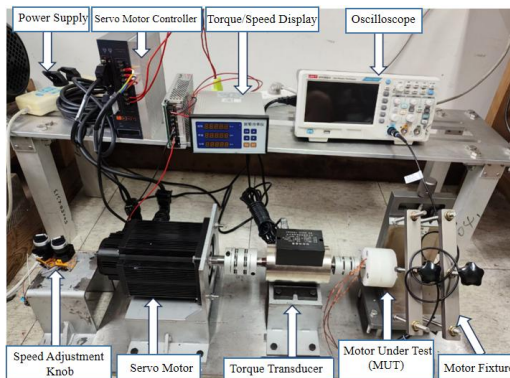


Figure 14: Test bench for back-EMF constant measurement of the motor.

Table V presents a detailed comparison across all the measured values and their simulated counterparts. The errors for resistance, inductance, and the back-EMF constant were all within 7.7%. Thus, the motor design is reasonable, the manufacturing process is sound, and the requirements for engineering applications are met.

Table V: Comparison of the measured and finite element analysis values for the motor parameters.

Motor parameter	Unit	Measured value	FEA value	Error
Phase resistance	Ω	0.42	0.44	4.8 %
Phase inductance	μH	23.55	25.31	7.5 %
No-load back-EMF constant	V/krpm	6.24	6.72	7.7 %

4.2 Motor output performance test

A motor performance test bench was constructed to measure the output torque and power under rated operating conditions (Fig. 15). The experimentally measured peak torque was 1.1 N·m, which deviated by 5.53 % from the simulated value of 1.16 N·m. The measured output power was 365 W, corresponding to a 4.3 % error compared with the optimization target of 381 W. The test results demonstrate that the performance of the optimized motor meets the design requirements.

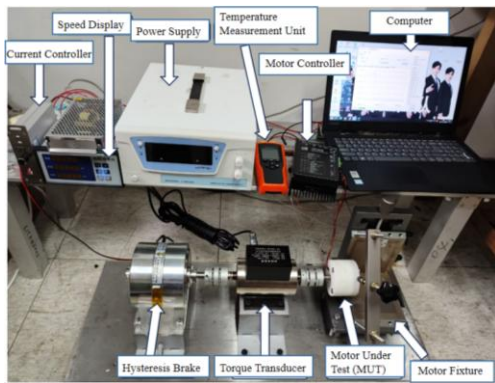


Figure 15: Motor performance test bench.

4.3 Temperature rise test

Fig. 16 shows a prototype of the optimized cooling channel. K-type thermocouples were embedded at key positions on the stator windings and core. A micro-self-priming pump was used to supply water to the channel at a controlled flow rate of 2 L/min. The motor was operated for specified durations under rated, peak torque, and peak speed conditions. The specific test procedures and results are as follows:

Rated operating conditions (3000 rpm, 1.0 N·m): The temperature stabilized after approximately 1000 s of operation. The maximum winding temperature reached 50 °C, which is in good agreement with the simulated value of 49.6 °C.

Peak torque condition (3000 rpm, 2.0 N·m): After 1200 s of operation, the maximum winding temperature was 65 °C. The cooling system remained effective under overload conditions.

Peak speed condition (4500 rpm, 1.0 N·m): The temperature increase rate increased significantly. The winding temperature increased to 88 °C after 200 s of operation. This trend suggests a need for enhanced heat dissipation or limited continuous operation time under extreme conditions.

The experimentally observed temperature trends, which were consistent with the simulation results, validated the established model and the optimization methodology.

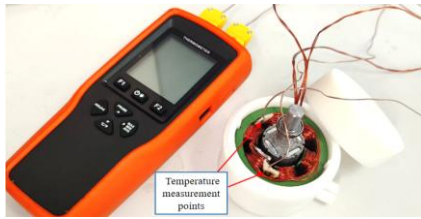


Figure 16: Temperature measurement points on the motor stator.

5. CONCLUSION AND FUTURE WORK

This study addressed the thermal-dissipation bottleneck of PMSMs for integrated pumps by establishing loss models, performing FSI-based simulations for structural optimization, and conducting multi-condition experimental validation. The main conclusions are as follows:

(1) Using the loss model and the FSI simulation framework, multiple primary–secondary channel configurations were compared in terms of flow and heat transfer behaviour. The full-spiral primary channel combined with a radial Z-shaped secondary channel (right inlet/left outlet) was optimal. It reduced the maximum winding temperature to 49.6 °C and satisfied thermal safety requirements for high-power-density operation.

(2) Multi-condition experiments confirmed the model accuracy and engineering feasibility. At rated conditions, the winding-temperature error between simulation and measurement was 0.8 %, and all key parameter errors were below 8 %. At the peak-torque condition (3000 rpm, 2.0 N·m), the maximum winding temperature reached 65 °C while maintaining safe operation.

Overall, the proposed closed-loop methodology – coordinated channel design, simulation-driven optimization, and multi-condition validation – enhances heat dissipation and power density for integrated pump motors. For ultra-high-speed operation (e.g., 4500 rpm), further improvements are required. Future work will focus on enhanced cooling concepts, higher-fidelity transient multi-physics coupling, and adaptive cooling control.

ACKNOWLEDGEMENT

The study was supported by the University Excellent Young Talents Cultivation Program (YQYB202310), and the Natural Science Foundation of Hefei City (HZR2502).

REFERENCES

- [1] Han, B.; He, Z.; Zhang, X.; Liu, X.; Wen, T.; Zheng, S. (2020). Loss estimation, thermal analysis, and measurement of a large-scale turbomolecular pump with active magnetic bearings, *IET Electric Power Applications*, Vol. 14, No. 7, 1283-1290, doi:[10.1049/iet-epa.2020.0037](https://doi.org/10.1049/iet-epa.2020.0037)
- [2] Wu, S.; Li, Z.; Tong, W. (2023). Research on thermal calculation and end winding heat conduction optimization of low speed high torque permanent magnet synchronous motor, *CES Transactions on Electrical Machines and Systems*, Vol. 7, No. 4, 397-403, doi:[10.30941/CESTEMS.2023.00039](https://doi.org/10.30941/CESTEMS.2023.00039)
- [3] Liu, Y.; Zhang, Z. (2022). Magnetic-thermal coupling simulation study of oil-cooled motor, *Automobile Technology*, Vol. 53, No. 11, 41-46, doi:[10.19620/j.cnki.1000-3703.20220790](https://doi.org/10.19620/j.cnki.1000-3703.20220790)
- [4] Yang, L.; Gao, T.; Ai, C.; Kong, X. (2024). Thermal analysis of stator iron-core-less PMBLDC motors considering both winding eddy and circulating current losses, *IEEE Access*, Vol. 12, 49791-49803, doi:[10.1109/ACCESS.2024.3384868](https://doi.org/10.1109/ACCESS.2024.3384868)
- [5] Ragi, K.; Sajith, V.; Kumaravel, S.; Meti, B. (2025). Thermal performance study of an electric-motor using innovative indirect cooling methods, *International Research Journal on Advanced Science Hub*, Vol. 7, No. 12, 1194-1205, doi:[10.47392/irjash.2025.133](https://doi.org/10.47392/irjash.2025.133)
- [6] Wang, L.; Li, Y.; Marignetti, F.; Boglietti, A. (2021). Coupled fluid-solid heat transfer of a gas and liquid cooling PMSM including rotor rotation, *IEEE Transactions on Energy Conversion*, Vol. 37, No. 1, 443-453, doi:[10.1109/tec.2021.3087831](https://doi.org/10.1109/tec.2021.3087831)

- [7] Yu, X.; Chen, D.; Wu, X.; Ai, M. (2024). The influence of loss distribution on the temperature field of high-speed induction motor, *IEEE Access*, Vol. 12, 40196-40203, doi:[10.1109/ACCESS.2024.3373544](https://doi.org/10.1109/ACCESS.2024.3373544)
- [8] Razani, A.; Rahbarimagham, H.; Zeinoddini-Meymand, H.; Hadi, M. (2025). Improving efficiency of SMC based IFOC drive for induction motor applying MRAS based adaptive loss model control, *Scientific Reports*, Vol. 15, Paper 39277, 33 pages, doi:[10.1038/s41598-025-23110-y](https://doi.org/10.1038/s41598-025-23110-y)
- [9] Liu, L.; Yin, W.; Guo, Y. (2024). Hybrid mechanism-data-driven iron loss modelling for permanent magnet synchronous motors considering multiphysics coupling effects, *IET Electric Power Applications*, Vol. 18, No. 12, 1833-1843, doi:[10.1049/elp2.12530](https://doi.org/10.1049/elp2.12530)
- [10] Jenkins, C.; Jones-Jackson, S.; Zaher, I.; Pietrini, G.; Rodriguez, R.; Cotton, J.; Emadi, A. (2023). Innovations in axial flux permanent magnet motor thermal management for high power density applications, *IEEE Transactions on Transportation Electrification*, Vol. 9, No. 3, 4380-4405, doi:[10.1109/TTE.2023.3242698](https://doi.org/10.1109/TTE.2023.3242698)
- [11] Xie, Y.; Zhao, X.; Cai, W.; Qi, G.; Wang, Z.; Zhang, Y.; Yang, Y. (2024). Design and optimisation of oil injection pipe cooling structure for permanent magnet synchronous motors in hybrid electric vehicles, *IET Electric Power Applications*, Vol. 18, No. 3, 345-355, doi:[10.1049/elp2.12393](https://doi.org/10.1049/elp2.12393)
- [12] Wu, C.; Li, C.; Wei, X.; Yang, J.-L.; Chen, L. (2025). Design optimization of the structure of fishbone channels in a battery liquid cooling plate, *Energy Storage and Saving*, Vol. 4, No. 3, 252-263, doi:[10.1016/j.enss.2025.05.001](https://doi.org/10.1016/j.enss.2025.05.001)
- [13] Acquaviva, A.; Skoog, S.; Thiringer, T. (2021). Design and verification of in-slot oil-cooled tooth coil winding PM machine for traction application, *IEEE Transactions on Industrial Electronics*, Vol. 68, No. 5, 3719-3727, doi:[10.1109/TIE.2020.2985009](https://doi.org/10.1109/TIE.2020.2985009)
- [14] Srinivasan, C.; Yang, X.; Schlautman, J.; Wang, D.; Gangaraj, S. (2020). Conjugate heat transfer CFD analysis of an oil cooled automotive electrical motor, *SAE International Journal of Advances and Current Practices in Mobility*, Vol. 2, No. 4, 1741-1753, doi:[10.4271/2020-01-0168](https://doi.org/10.4271/2020-01-0168)
- [15] Park, M. H.; Kim, S. C. (2023). Development and validation of lumped parameter thermal network model on rotational oil spray cooled motor for electric vehicles, *Applied Thermal Engineering*, Vol. 225, Paper 120176, 14 pages, doi:[10.1016/j.applthermaleng.2023.120176](https://doi.org/10.1016/j.applthermaleng.2023.120176)
- [16] Chen, W.; Luo, Q.; Cai, Z.; Wang, C. (2024). Temperature field analysis and cooling structure optimization of permanent magnet linear synchronous motor, *Thermal Science and Engineering Progress*, Vol. 50, Paper 102532, 10 pages, doi:[10.1016/j.tsep.2024.102532](https://doi.org/10.1016/j.tsep.2024.102532)
- [17] Niu, L. Q.; Wang, Y. F.; Li, Z.; Miao, W. Y.; Li, X. R. (2025). Thermal simulation of UAV Li-Po batteries under abnormal ageing conditions, *International Journal of Simulation Modelling*, Vol. 24, No. 2, 309-320, doi:[10.2507/IJSIMM24-2-730](https://doi.org/10.2507/IJSIMM24-2-730)
- [18] Liu, B.; Yu, Z.; Fu, J. (2024). Thermal modeling and analysis of a HPMSM coupling with magnetic bearings, *IEEE Access*, Vol. 12, 81362-81373, doi:[10.1109/ACCESS.2024.3410326](https://doi.org/10.1109/ACCESS.2024.3410326)
- [19] Zhang, J.; Zhang, J.; Liu, Z. (2024). Numerical evaluation of the heat transfer performance of water-cooled system for electric vehicle drive motor based on the field synergy principle, *Thermal Science*, Vol. 28, No. 2, Part A, 823-835, doi:[10.2298/TSCI230422164Z](https://doi.org/10.2298/TSCI230422164Z)
- [20] Du, J. J.; Liu, B. R.; Yang, X. D.; Chen, Y. G.; Zhang, W. (2025). Dynamic analysis of rotor and machine structure in ultra-high-speed PMSM, *International Journal of Simulation Modelling*, Vol. 24, No. 3, 497-508, doi:[10.2507/IJSIMM24-3-CO11](https://doi.org/10.2507/IJSIMM24-3-CO11)
- [21] Gözüaçık, E.; Akar, M. (2025). Multi-physics and multi-objective design of an axial flux permanent magnet-assisted synchronous reluctance motor for use in electric vehicles, *Machines*, Vol. 13, No. 7, Paper 555, 18 pages, doi:[10.3390/machines13070555](https://doi.org/10.3390/machines13070555)
- [22] Zhao, P.; Yu, Y. (2022). Analysis of influence of permanent magnet demagnetization on motor temperature rise, *Journal of Physics: Conference Series*, Vol. 2395, Paper 012022, 7 pages, doi:[10.1088/1742-6596/2395/1/012022](https://doi.org/10.1088/1742-6596/2395/1/012022)
- [23] Han, B.; Peng, S.; He, Z.; Liu, X.; Zhang, X. (2020). Eddy current loss calculation and thermal analysis of high-speed motor winding in magnetically suspended control moment gyroscope, *Optics and Precision Engineering*, Vol. 28, No. 1, 130-140